

In-situ tunneling control in photonic potentials by Rashba-Dresselhaus spin-orbit coupling

Rafał Mirek,^{1,*} Pavel Kokhanchik,^{2,*} Darius Urbonas,¹ Ioannis Georgakilas,¹ Marcin Muszyński,³ Piotr Kapuściński,³ Przemysław Oliwa,³ Barbara Piętka,³ Jacek Szczytko,³ Michael Forster,⁴ Ullrich Scherf,⁴ Przemysław Morawiak,⁵ Wiktor Piecek,⁵ Przemysław Kula,⁶ Dmitry Solnyshkov,^{2,7} Guillaume Malpuech,² Rainer F. Mahrt,¹ and Thilo Stöferle¹

¹IBM Research Europe - Zurich, Säumerstrasse 4, Rüschlikon, Switzerland[†]

²Université Clermont Auvergne, Clermont Auvergne INP, CNRS, Institut Pascal, F-63000 Clermont-Ferrand, France

³Institute of Experimental Physics, Faculty of Physics, University of Warsaw, Poland

⁴Macromolecular Chemistry Group and Wuppertal Center for Smart Materials & Systems (CM@S), Bergische Universität Wuppertal, Gauss Strasse 20, 42119 Wuppertal, Germany

⁵Institute of Applied Physics, Military University of Technology, Warsaw, Poland

⁶Institute of Chemistry, Military University of Technology, Warsaw, Poland

⁷Institut Universitaire de France (IUF), 75231 Paris, France

The tunability of individual coupling amplitudes in photonic lattices is highly desirable for photonic Hamiltonian engineering and for studying topological transitions *in situ*. In this work, we demonstrate the tunneling control between individual lattice sites patterned inside an optical microcavity. The tuning is achieved by applying a voltage to a liquid crystal microcavity possessing photonic Rashba-Dresselhaus spin-orbit coupling. This type of spin-orbit coupling emerges due to the high birefringence of the liquid crystal material and constitutes an artificial gauge field for photons. The proposed technique can be combined with strong-light matter coupling and non-Hermitian physics already established in liquid crystal microcavities.

INTRODUCTION

Topological photonics [1, 2], which has gained enormous interest in recent decades, involves numerous effects like the creation of one-way edge states [3–7], structures for topological lasing [8–12], tuning of the topology [13], guiding of light [14–16], non-Abelian physics [17–21] (including the non-Abelian Hofstadter model [22]), Klein tunneling in topological structures [23], and chiral zero mode formation at Weyl points [24] that can be described in terms of artificial gauge fields [18, 25], in real [25] and reciprocal space [26]. In the frameworks of Floquet engineering [27–29], synthetic dimensions [30–32], and spin-orbit coupling (SOC) [17, 19, 33, 34], often creative but sophisticated fabrication geometries are used to build an artificial gauge field. Various realizations of artificial gauge fields are based on lattice coupling control techniques, e.g., amplitude control techniques, as in the case of Landau levels observed in strained lattices [35–37], or phase control techniques, allowing to realize the Harper-Hofstadter model in coupled resonator arrays [38, 39] and topological insulator lasers [11, 40]. Most of these techniques do not allow controlling the couplings *in situ*, that is, to tune them during the experiment, which limits the versatility and the scope of possible applications.

Lately, a new type of photonic SOC called Rashba-Dresselhaus spin-orbit coupling (RDSOC) was developed in highly birefringent optical microcavities arising from the coupling of modes of orthogonal polarization and opposite parity [41, 42]. Similar SOC has also been obtained in microwave metamaterials [43]. Since then, photonic

RDSOC in microcavities has been studied extensively and various effects such as persistent spin helix [44, 45], tunable Berry curvature [46, 47], polariton lasing [48, 49], spin Hall effect [50], and polariton striped phase [51], have been demonstrated. In a bare liquid crystal (LC) microcavity without any lattice, the RDSOC can already be described as a gauge potential of Abelian [41, 42] or non-Abelian nature [19, 52], depending on the presence of a coupling between circular components. This makes RDSOC more similar to gauge fields for electrons [53, 54] than to other synthetic gauge fields in photonics, which are usually achieved by lattice coupling engineering [55]. Therefore, we inverse the paradigm and study how the photonic artificial gauge field in the form of RDSOC affects the lattice couplings, providing a useful tool for fundamental and applied studies, because the variation of the couplings allows obtaining different emergent Hamiltonians and tuning them across transitions. In a previous work by some of us, two different regimes of coupling control, i.e., amplitude and phase control, have already been demonstrated theoretically [56]. It was shown that the former allows to realize a Su-Schrieffer-Heeger (SSH) chain with a topological phase transition driven by a voltage applied to the microcavity, while the latter provides a way to implement the spinful Harper-Hofstadter model. However, an experimental implementation with a demonstration of *in situ* coupling control has been missing so far.

In this work, we experimentally demonstrate coupling amplitude control achieved through RDSOC. We start by studying a single Gaussian trap (ST) in an LC mi-

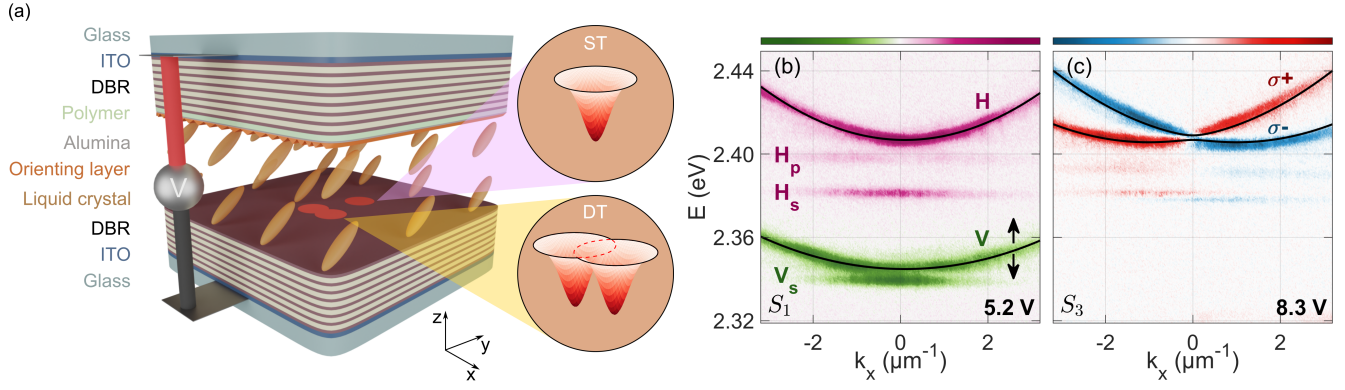


Figure 1. (a) Scheme of LC microcavity with ST and DT potentials; experimentally measured dispersion of ST for (b) 5.2 V and (c) 8.3 V shown as S_1 and S_3 Stokes parameters, respectively; the data is nonlinearly transformed and saturated in order to enhance the visibility of localized states marked as V_s , H_s and H_p ; the colorbars are in arb. units; black solid lines show the fit of continuous modes (H and V in (b), σ^+ and σ^- in (c)) by Hamiltonian (1); black double-headed arrow depicts the tunability of V mode. See parameters in [57].

croavity. We demonstrate coupling by RDSOC between orthogonally linearly-polarized localized s and p states of ST. Next, we study a double Gaussian trap (DT) and show how the coupling amplitude between two collinearly polarized localized s states can be controlled through RDSOC. The coupling can be continuously tuned with applied voltage, which is an important step forward even with respect to previous theoretical predictions [56]. This kind of tunable coupling control is hard to achieve in any other optical microcavity realization. An important perspective is opened by the possibility to reduce the coupling to zero and then to invert its sign by increasing the RDSOC. This realizes a topological transition observable as a swap of symmetric and anti-symmetric states in the microcavity spectrum.

RESULTS

The studied LC microcavity sample is displayed in Fig. 1(a). The detailed structure and measurement setup are presented in [57]. To study the optical properties, white light transmission measurements at room temperature have been carried out. The microcavity with distributed Bragg reflectors (DBR) filled with several micrometer thick layer of nematic liquid crystal (LC) naturally possesses longitudinal modes which can be numbered with an integer corresponding to the number of field antinodes. The orientation of the molecular director in the yz plane can be controlled via a voltage applied to the indium tin oxide (ITO) electrodes, resulting in tuning of the effective permittivity ε_{yy} , while ε_{xx} remains constant. At high voltage, the LC molecules are oriented along the cavity axis z , so that H and V modes with the same order number N are in resonance [41]. Due to the large birefringence of the LC material, while changing voltage, the orthogonally linearly polarized eigenmodes

can be significantly detuned, so that the modes of different numbers can approach each other. In the regime where the H-polarized N th mode and the V-polarized $(N+1)$ th mode are energetically close to each other, the coupling of these bands leads to the RDSOC effect [41, 42]. Here, an effective 1D two-band Hamiltonian along the direction perpendicular to the plane of the director rotation, in the basis defined by the two linearly-polarized H and V modes, reads [41]:

$$H(k_x) = \frac{\hbar^2 k_x^2}{2M} \mathbb{I} + \left(\frac{\hbar^2 k_x^2}{2m} + 2\alpha k_x \right) \sigma_x + \delta \sigma_1, \quad (1)$$

with $1/M = (1/m_H + 1/m_V)/2$, $1/m = (1/m_H - 1/m_V)/2$, where m_H (m_V) is the mass of the H-(V-)polarized mode, α – the RDSOC parameter, δ – the (linear) detuning between N th H and $(N+1)$ th V modes, k_x – the wavevector component along the RDSOC direction. Finally, $\sigma_1 = (\mathbb{I} - \sigma_z)/2$, where \mathbb{I} is the identity matrix, $\sigma_{x,z}$ are the Pauli matrices. σ_1 is used because the applied voltage shifts only the V-polarized band.

In Fig. 1, we show the dispersion measured at the position of an ST for different voltages. At small voltages, the detuning δ between the two linear polarizations is large, and therefore, the eigenmodes are predominantly linearly polarized. It is clearly visible when plotting the first Stokes parameter (degree of linear polarization) S_1 (Fig. 1(b)). Along with continuous parabolic cavity modes, well described by the Hamiltonian (1), we observe the localized states. Due to the contrast in H and V effective refractive indices, the effective potential depth of the ST is different for H and V. As a result, a single localized state is observed for V and two localized states for H. We call them s and p levels, in analogy with atomic orbitals.

For higher voltages (around 8.3 V), the V mode of $(N+1)$ th order approaches the H mode of N th order,

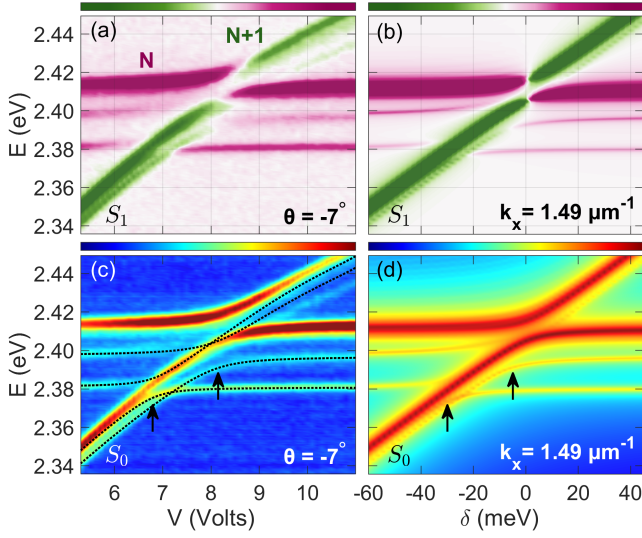


Figure 2. Energy-voltage diagrams showing the near-resonant regime between N th H mode and $(N+1)$ th V mode in an ST. (a,c) Experimental and (b,d) numerical results represented as (a,b) linear polarization degree S_1 and (c,d) total intensity S_0 ; the detection angle of experimental data $\theta = -7^\circ$ corresponds to $k_x = 1.49 \mu\text{m}^{-1}$ of the numerical simulation; the data is nonlinearly transformed and saturated in order to enhance visibility of localized states; the colorbars are in arb. units; black arrows in (c,d) mark anticrossing points; black dotted lines in (c) show the energies obtained by diagonalizing tight-binding Hamiltonian (2). See simulation parameters and other Stokes components for full 0-11 V voltage range in [57].

and the RDSOC contribution $2\alpha k_x$ starts to dominate over the splitting δ between the linearly-polarized modes (Fig. 1(c)). In this regime, the eigenmodes are mostly circularly polarized and split along k_x , which is visible when plotting the third Stokes parameter (degree of circular polarization) S_3 . Indeed, the $2\alpha k_x \sigma_x$ term produces an effect similar to the optical activity [42].

We measured the dispersion at the position of an ST for the set of voltages between 0 V and 11 V. The results are shown in Fig. 2(a) in an energy-voltage plot for a fixed angle of detection of -7° corresponding to $k_x = 1.49 \mu\text{m}^{-1}$ (which optimizes the simultaneous visibility of both s and p localized states). The tunability of the V mode with voltage is well visible in this type of diagram. The experimental results can be reproduced by numerically solving the stationary Schrödinger equation with the Hamiltonian (1) as displayed in Fig. 2(b). From the experimentally measured total intensity in Fig. 2(c), one can infer that localized states anticross at the positions highlighted by black arrows, corroborated by numerical results (Fig. 2(d)). This anticrossing is a manifestation of RDSOC-mediated coupling between particular localized states of H and V. The absolute value of the matrix elements of this coupling can be generally written as $\beta = |\langle H_l | 2\alpha k_x | V_{l'} \rangle|$, with $l(l') = \{s, p, \dots\}$ represent-

ing the quantum number of a localized state. Since the RDSOC term is linear in k_x , it couples only the localized states of opposite parity (s and p in our case). While the V_p state was not visible in Fig. 1(b), it appears when H and V are close to resonance, and so it can couple with the other states which are always visible. Therefore, the tight-binding model for localized states of an ST in the basis $(|H_s\rangle |H_p\rangle |V_s\rangle |V_p\rangle)^T$ can be written as:

$$H_{ST} = \begin{pmatrix} E_{H_s} & 0 & 0 & -i\beta_{ST,2} \\ 0 & E_{H_p} & i\beta_{ST,1} & 0 \\ 0 & -i\beta_{ST,1} & E_{V_s} + \delta & 0 \\ i\beta_{ST,2} & 0 & 0 & E_{V_p} + \delta \end{pmatrix}. \quad (2)$$

Two different coupling coefficients $\beta_{ST,1(2)}$ give rise to two anticrossing points observed in Fig. 2(c,d). By diagonalizing the tight-binding Hamiltonian (2), we obtain a good correspondence with experimental results (black dotted lines in Fig. 2(c)).

We now turn to the consideration of the DT potential. The dispersions for negative and positive linear detunings are shown in Fig. 3(a,b), respectively. Now, each state of an ST is split into two states, since the traps forming the DT are coupled by tunneling. We dub the resulting states "even" and "odd" (superscript notations e and o), depending on the symmetry of the corresponding DT eigenstate in real space. For both H and V modes, we observe three localized states. The coupling between different localized states is described by the same matrix elements with β introduced above. Note that the energy splitting between H_s^e and H_s^o localized states is different for panels (a) and (b) in Fig. 3. Moreover, it changes continuously with voltage (Fig. 3(e)). The effect is especially pronounced when approaching the resonance. At the same time, the polarization of the states is mostly conserved, which is confirmed by S_1 both in the experiment (Fig. 3(c)) and numerical simulation (Fig. 3(d)). Since the uncoupled states in both traps are degenerate, the energy splitting between the DT states can be written as $2j$, where j is a tunneling coefficient. This result can be interpreted as a continuous control of the effective tunneling by the applied voltage due to the RDSOC: $j = j(V)$.

To confirm this hypothesis, we built a 6x6 tight-binding model (see [57]) taking into account all localized states, and then using perturbation theory up to the 2nd order in the limit $|\delta| \gg \max|\Delta E_{ij}|, \beta, |j_0|$, where ΔE_{ij} is a difference between i th and j th localized states and j_0 is the tunneling in the absence of RDSOC, we reduced it to an effective 2×2 Hamiltonian including only $(|H_s^l\rangle |H_s^r\rangle)^T$ basis states (left and right wells in a DT):

$$H_{DT} = \begin{pmatrix} E'_{H_s}(\delta) & -j(\delta) \\ -j(\delta) & E'_{H_s}(\delta) \end{pmatrix}, \quad (3)$$

with $E'_{H_s}(\delta)$ – the detuning-dependent modified energy of an ST H_s state (see [57]). Importantly, we obtain an

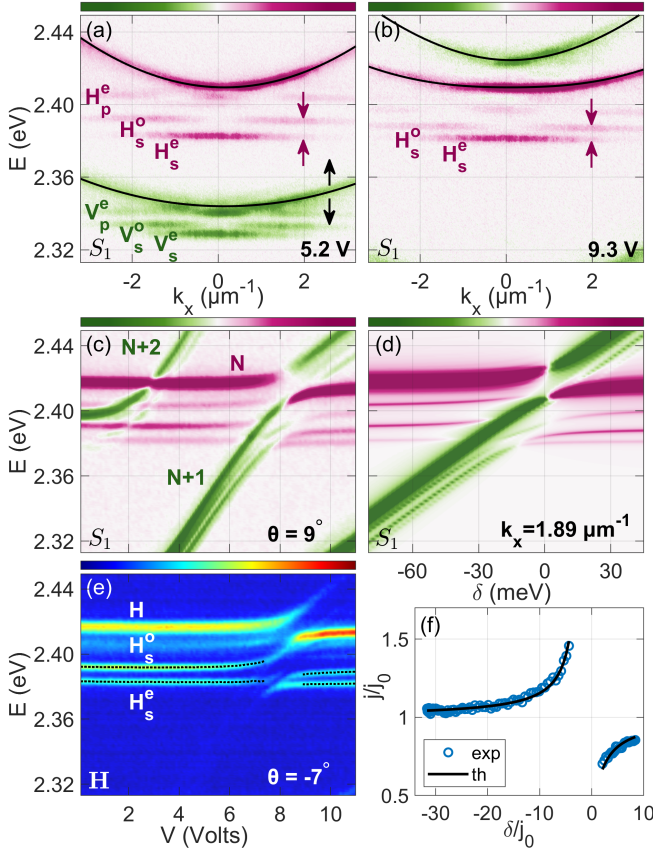


Figure 3. Experimentally measured dispersion of a DT for (a) 5.2 V and (b) 9.3 V shown as S_1 Stokes parameter; black solid lines show the fit by Hamiltonian (1); black double-headed arrow depicts the tunability of V mode; purple arrows mark the spectral distance between H_s^e and H_s^o ; (c,e) experimental and (d) numerical results represented as (c,d) S_1 linear polarization degree and (e) H intensity; black dotted lines in (e) show the extracted energies of H_s^e and H_s^o localized states; the data in (a-e) is nonlinearly transformed and saturated in order to enhance the visibility of localized states; the colorbars are in arb. units; (f) effective coupling coefficient between H_s^e and H_s^o localized states extracted from the experiment (blue dots) and fitted by $j(\delta)$ (black line). See simulation parameters and other Stokes components in [57].

expression for the detuning-dependent effective tunneling:

$$j(\delta) = j_0 - \frac{\beta_{DT,2}^2}{2(E_{V_p^e} - E_{H_s} + \delta)} \quad (4)$$

where $\beta_{DT,2} = |\langle H_s^o | 2\alpha k_x | V_p^e \rangle|$, E_{H_s} and $E_{V_p^e}$ are the energies of ST H_s and DT V_p^e states, respectively. The effective tunneling extracted from the experiment is shown as blue points in Fig. 3(f), while the fitting of this data with $j(\delta)$ is illustrated by a solid black line. We, therefore, conclude that the hyperbolic dependence of the tunneling j on the detuning δ (directly controlled by the voltage) given by Eq. (4) is confirmed by the experiment. The

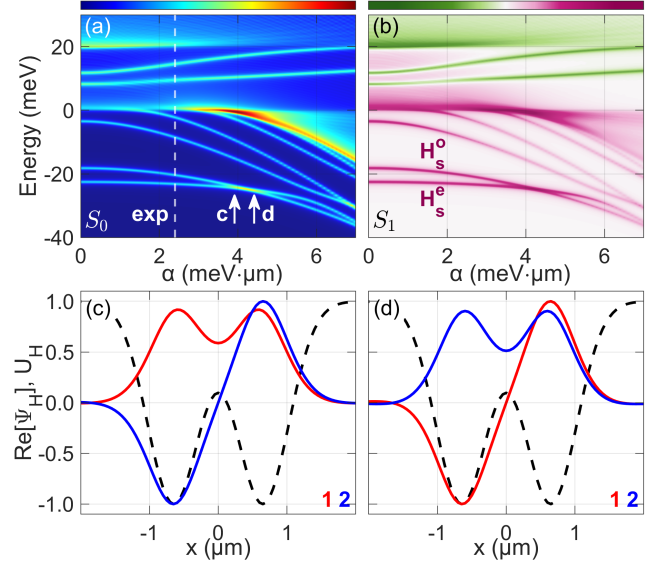


Figure 4. Spectrum of a DT depending on RDSOC parameter α showing a spectral inversion between H_s^e and H_s^o localized states in (a) total intensity S_0 and (b) linear polarization degree S_1 ; the colorbars are in arb. units; real part of H-polarized wavefunction component $\text{Re}[\Psi_H]$ of the lowest (1, red) and the second lowest (2, blue) localized states (c) before and (d) after level inversion; black dashed line shows a potential U_H for H; $\text{Re}[\Psi_H]$ and U_H units are normalized; white dashed line in (a) shows the experimental value of RDSOC parameter α presented in Fig. 3. See parameters in [57].

total change of $j(\delta)$ is from $0.7j_0$ to $1.45j_0$, exceeding a factor 2. This change is only possible if the absolute value of the RDSOC matrix element $\beta_{DT,2}$ is non-zero. Thus, the RDSOC-mediated coupling of the s and p states plays a crucial role in the control of the coupling between the two traps.

Another remarkable property of the effective coupling $j(\delta)$ is a minus sign allowing, in principle, to suppress the effective coupling down to zero or even to invert its sign. The inversion of the coupling sign is inextricably linked with a topological transition manifesting itself in the experiment as a spectral swap between e and o localized states. In lattices, this exchange of the states of different symmetry is associated with a topological transition [58]. In Fig. 4 we demonstrate this effect in numerical simulations. Figs. 4(a,b) show the evolution of the spectrum with increasing RDSOC constant α . At $\alpha \approx 4 \text{ meV} \cdot \mu\text{m}$, the H_s^e and H_s^o localized states cross in energy. By looking at the structure of the lowest (1) and second lowest (2) states in real space before the crossing (Fig. 4(c)) and after the crossing (Fig. 4(d)), one can easily notice the inversion between the e and o states. At the same time, the polarization of these states is mostly conserved, as confirmed by the degree of linear polarization S_1 (Fig. 4(b)).

In our DT experiment (Fig. 3), the value of α is $2.4 \text{ meV} \cdot \mu\text{m}$, which does not allow us to observe this topo-

logical transition experimentally (white dashed line in Fig. 4(a)). The simplest way to achieve it in future experiments is to utilize LC materials with higher birefringence.

DISCUSSION AND CONCLUSIONS

Along with an abundance of physical phenomena, microcavities allow studying various lattice models, often in the context of topological photonics. Nowadays, the most common techniques for lattice engineering in planar microcavities are micropillar etching [59, 60], where the tunneling in the presence of spin-orbit coupling has also been studied [61], and ballistical coupling [62]. Both of these techniques lack a simple tunability for the lattice couplings. This reduces the range of models to be investigated, and, probably more importantly, does not provide dynamical access to the transitions between different topological phases of the model. The technique of coupling amplitude and sign control suggested in the present work, along with the phase control discussed before [56], allows accessing richer topological physics in optical microcavities. This approach can be further extended to the domains of strong light-matter interaction, non-linear physics, or non-Hermitian physics, since all necessary ingredients are available in LC microcavities. Furthermore, the presented coupling control and inversion can be applied in cold atom systems in addition to the existing opportunities [63], since RDSOC is broadly studied there [64].

In this work, we studied the localized states in LC microcavity in the presence of RDSOC. We demonstrated experimentally the coupling between ST localized states of different parity (s and p). We then studied experimentally the DT system and showed how the effective tunneling between the traps can be continuously controlled by the voltage applied to the LC microcavity thanks to the presence of the mentioned RDSOC-mediated sp coupling. Finally, in addition to the coupling amplitude control, we demonstrated theoretically that the coupling sign can be inverted, which shows up as a topological transition in the LC microcavity spectrum.

ACKNOWLEDGMENTS

We thank the team of the IBM Binnig and Rohrer Nanotechnology Center and D. Caimi for support with the sample fabrication. This work was supported by the European Union's Horizon 2020 program, through a FET Open research and innovation action under grant agreements No. 964770 (TopoLight) and EU H2020 MSCA-ITN project under grant agreement No. 956071 (AppQInfo). Additional support was provided by the ANR Labex GaNext (ANR-11-LABX-0014), the ANR

program "Investissements d'Avenir" through the IDEX-ISITE initiative 16-IDEX-0001 (CAP 20-25), the ANR project MoirePlusPlus, and the ANR project "NEWAVE" (ANR-21-CE24-0019).

* These authors contributed equally to this letter.

† rafal.mirek@ibm.com

- [1] L. Lu, J. D. Joannopoulos, and M. Soljačić, *Nature Photonics* **8**, 821 (2014).
- [2] H. Price, Y. Chong, A. Khanikaev, H. Schomerus, L. J. Maczewsky, M. Kremer, M. Heinrich, A. Szameit, O. Zilberberg, Y. Yang, *et al.*, *Journal of Physics: Photonics* **4**, 032501 (2022).
- [3] F. D. M. Haldane and S. Raghu, *Physical Review Letters* **100**, 013904 (2008).
- [4] Z. Wang, Y. Chong, J. D. Joannopoulos, and M. Soljačić, *Nature* **461**, 772 (2009).
- [5] A. V. Nalitov, D. D. Solnyshkov, and G. Malpuech, *Physical Review Letters* **114**, 116401 (2015).
- [6] S. Klemmt, T. Harder, O. Egorov, K. Winkler, R. Ge, M. Bandres, M. Emmerling, L. Worschech, T. Liew, M. Segev, *et al.*, *Nature* **562**, 552 (2018).
- [7] A. Slobozhanyuk, S. H. Mousavi, X. Ni, D. Smirnova, Y. S. Kivshar, and A. B. Khanikaev, *Nature Photonics* **11**, 130 (2017).
- [8] D. D. Solnyshkov, A. V. Nalitov, and G. Malpuech, *Physical Review Letters* **116**, 046402 (2016).
- [9] P. St-Jean, V. Goblot, E. Galopin, A. Lemaître, T. Ozawa, L. Le Gratiet, I. Sagnes, J. Bloch, and A. Amo, *Nature Photonics* **11**, 651 (2017).
- [10] B. Bahari, A. Ndao, F. Vallini, A. El Amili, Y. Fainman, and B. Kanté, *Science* **358**, 636 (2017).
- [11] M. A. Bandres, S. Wittek, G. Harari, M. Parto, J. Ren, M. Segev, D. N. Christodoulides, and M. Khajavikhan, *Science* **359**, 1231 (2018).
- [12] J.-H. Choi, W. E. Hayenga, Y. G. Liu, M. Parto, B. Bahari, D. N. Christodoulides, and M. Khajavikhan, *Nature Communications* **12**, 3434 (2021).
- [13] Z. A. Kudyshev, A. V. Kildishev, A. Boltasseva, and V. M. Shalae, *ACS photonics* **6**, 1922 (2019).
- [14] Y. Lumer, M. A. Bandres, M. Heinrich, L. J. Maczewsky, H. Herzig-Sheinfux, A. Szameit, and M. Segev, *Nature Photonics* **13**, 339 (2019).
- [15] H. Chalabi, S. Barik, S. Mittal, T. E. Murphy, M. Hafezi, and E. Waks, *Optica* **7**, 506 (2020).
- [16] A. Vakulenko, S. Kiriushchikina, D. Smirnova, S. Guldala, F. Komissarenko, A. Alù, M. Allen, J. Allen, and A. B. Khanikaev, *Nature Communications* **14**, 4629 (2023).
- [17] H. Terças, H. Flayac, D. D. Solnyshkov, and G. Malpuech, *Physical Review Letters* **112**, 066402 (2014).
- [18] Y. Chen, R.-Y. Zhang, Z. Xiong, Z. H. Hang, J. Li, J. Q. Shen, and C. T. Chan, *Nature Communications* **10**, 3125 (2019).
- [19] L. Polimeno, A. Fieramosca, G. Lerario, L. De Marco, M. De Giorgi, D. Ballarini, L. Dominici, V. Ardizzone, M. Pugliese, C. Prontera, *et al.*, *Optica* **8**, 1442 (2021).
- [20] Q. Yan, Z. Wang, D. Wang, R. Ma, C. Lu, G. Ma, X. Hu, and Q. Gong, *Advances in Optics and Photonics* **15**, 907 (2022).

- (2023).
- [21] Y. Yang, B. Yang, G. Ma, J. Li, S. Zhang, and C. Chan, *Science* **383**, 844 (2024).
 - [22] Y. Yang, B. Zhen, J. D. Joannopoulos, and M. Soljačić, *Light: Science & Applications* **9**, 177 (2020).
 - [23] X. Ni, D. Putseladze, D. A. Smirnova, A. Slobozhanyuk, A. Alù, and A. B. Khanikaev, *Science Advances* **4** (2018).
 - [24] H. Jia, R. Zhang, W. Gao, Q. Guo, B. Yang, J. Hu, Y. Bi, Y. Xiang, C. Liu, and S. Zhang, *Science* **363**, 148 (2019).
 - [25] M. Aidelsburger, S. Nascimbene, and N. Goldman, *Comptes Rendus Physique* **19**, 394 (2018).
 - [26] H. M. Price, T. Ozawa, and I. Carusotto, *Physical Review Letters* **113**, 190403 (2014).
 - [27] M. C. Rechtsman, J. M. Zeuner, Y. Plotnik, Y. Lumer, D. Podolsky, F. Dreisow, S. Nolte, M. Segev, and A. Szameit, *Nature* **496**, 196 (2013).
 - [28] D. Hey and E. Li, *Royal Society Open Science* **5**, 172447 (2018).
 - [29] Z. Yang, E. Lustig, Y. Lumer, and M. Segev, *Light: Science & Applications* **9**, 128 (2020).
 - [30] T. Ozawa, H. M. Price, N. Goldman, O. Zilberberg, and I. Carusotto, *Physical Review A* **93**, 043827 (2016).
 - [31] E. Lustig, S. Weimann, Y. Plotnik, Y. Lumer, M. A. Bandres, A. Szameit, and M. Segev, *Nature* **567**, 356 (2019).
 - [32] A. Dutt, Q. Lin, L. Yuan, M. Minkov, M. Xiao, and S. Fan, *Science* **367**, 59 (2020).
 - [33] A. V. Nalitov, G. Malpuech, H. Terças, and D. D. Solnyshkov, *Physical Review Letters* **114**, 026803 (2015).
 - [34] C. Whittaker, T. Dowling, A. V. Nalitov, A. V. Yulin, B. Royall, E. Clarke, M. S. Skolnick, I. A. Shelykh, and D. N. Krizhanovskii, *Nature Photonics* **15**, 193 (2021).
 - [35] M. C. Rechtsman, J. M. Zeuner, A. Tünnermann, S. Nolte, M. Segev, and A. Szameit, *Nature Photonics* **7**, 153 (2013).
 - [36] O. Jamadi, E. Rozas, G. Salerno, M. Milićević, T. Ozawa, I. Sagnes, A. Lemaître, L. Le Gratiet, A. Harouri, I. Carusotto, *et al.*, *Light: Science & Applications* **9**, 144 (2020).
 - [37] R. Barczyk, L. Kuipers, and E. Verhagen, *Nature Photonics* **18**, 574–579 (2024).
 - [38] M. Hafezi, E. A. Demler, M. D. Lukin, and J. M. Taylor, *Nature Physics* **7**, 907 (2011).
 - [39] R. O. Umucalılar and I. Carusotto, *Physical Review A* **84**, 043804 (2011).
 - [40] G. Harari, M. A. Bandres, Y. Lumer, M. C. Rechtsman, Y. D. Chong, M. Khajavikhan, D. N. Christodoulides, and M. Segev, *Science* **359**, 1230 (2018).
 - [41] K. Rechcińska, M. Król, R. Mazur, P. Morawiak, R. Mirek, K. Łempicka, W. Bardyszewski, M. Matuszewski, P. Kula, W. Piecek, *et al.*, *Science* **366**, 727 (2019).
 - [42] J. Ren, Q. Liao, F. Li, Y. Li, O. Bleu, G. Malpuech, J. Yao, H. Fu, and D. Solnyshkov, *Nature Communications* **12**, 689 (2021).
 - [43] F. Liu, T. Xu, S. Wang, Z. H. Hang, and J. Li, *Advanced Optical Materials* **7**, 1801582 (2019).
 - [44] M. Król, K. Rechcińska, H. Sigurdsson, P. Oliwa, R. Mazur, P. Morawiak, W. Piecek, P. Kula, P. G. Lagoudakis, M. Matuszewski, *et al.*, *Physical Review Letters* **127**, 190401 (2021).
 - [45] M. Muszyński, M. Król, K. Rechcińska, P. Oliwa, M. Kędziora, K. Łempicka-Mirek, R. Mazur, P. Morawiak, W. Piecek, P. Kula, P. G. Lagoudakis, B. Piętka, and J. Szczytko, *Physical Review Applied* **17**, 014041 (2022).
 - [46] L. Polimeno, G. Lerario, M. De Giorgi, L. De Marco, L. Dominici, F. Todisco, A. Coriolano, V. Ardizzone, M. Pugliese, C. T. Prontera, *et al.*, *Nature Nanotechnology* **16**, 1349 (2021).
 - [47] K. Łempicka-Mirek, M. Król, H. Sigurdsson, A. Wincukiewicz, P. Morawiak, R. Mazur, M. Muszyński, W. Piecek, P. Kula, T. Stefaniuk, *et al.*, *Science Advances* **8**, eabq7533 (2022).
 - [48] Y. Li, X. Ma, X. Zhai, M. Gao, H. Dai, S. Schumacher, and T. Gao, *Nature Communications* **13**, 3785 (2022).
 - [49] T. Long, X. Ma, J. Ren, F. Li, Q. Liao, S. Schumacher, G. Malpuech, D. Solnyshkov, and H. Fu, *Advanced Science* **9**, 2203588 (2022).
 - [50] J. Liang, W. Wen, F. Jin, Y. G. Rubo, T. C. H. Liew, and R. Su, *Nature Photonics* **18**, 357 (2024).
 - [51] M. Muszyński, P. Kokhanchik, D. Urbonas, P. Kapusiński, P. Oliwa, R. Mirek, I. Georgakilas, T. Stöferle, R. F. Mahrt, M. Forster, U. Scherf, D. Dovzhenko, R. Mazur, P. Morawiak, W. Piecek, P. Kula, B. Piętka, D. Solnyshkov, G. Malpuech, and J. Szczytko, *arXiv preprint arXiv:2407.02406* (2024).
 - [52] P.-Q. Jin, Y.-Q. Li, and F.-C. Zhang, *Journal of Physics A: Mathematical and General* **39**, 7115 (2006).
 - [53] B. A. Bernevig, J. Orenstein, and S.-C. Zhang, *Physical Review Letters* **97**, 236601 (2006).
 - [54] J. D. Koralek, C. P. Weber, J. Orenstein, B. A. Bernevig, S.-C. Zhang, S. Mack, and D. Awschalom, *Nature* **458**, 610 (2009).
 - [55] G.-J. Tang, X.-T. He, F.-L. Shi, J.-W. Liu, X.-D. Chen, and J.-W. Dong, *Laser & Photonics Reviews* **16**, 2100300 (2022).
 - [56] P. Kokhanchik, D. Solnyshkov, T. Stöferle, B. Piętka, J. Szczytko, and G. Malpuech, *Physical Review Letters* **129**, 246801 (2022).
 - [57] See Supplemental Material.
 - [58] B. A. Bernevig, T. L. Hughes, and S.-C. Zhang, *science* **314**, 1757 (2006).
 - [59] S. Michaelis de Vasconcellos, A. Calvar, A. Dousse, J. Suffczyński, N. Dupuis, A. Lemaître, I. Sagnes, J. Bloch, P. Voisin, and P. Senellart, *Applied Physics Letters* **99** (2011).
 - [60] D. D. Solnyshkov, G. Malpuech, P. St-Jean, S. Ravets, J. Bloch, and A. Amo, *Optical Materials Express* **11**, 1119 (2021).
 - [61] V. Sala, D. D. Solnyshkov, I. Carusotto, T. Jacqmin, A. Lemaître, H. Terças, A. Nalitov, M. Abbarchi, E. Galopin, I. Sagnes, *et al.*, *Physical Review X* **5**, 011034 (2015).
 - [62] J. D. Töpfer, I. Chatzopoulos, H. Sigurdsson, T. Cookson, Y. G. Rubo, and P. G. Lagoudakis, *Optica* **8**, 106 (2021).
 - [63] N. P. Proukakis, D. W. Snoke, and P. B. Littlewood, *Universal Themes of Bose-Einstein Condensation* (Cambridge University Press, 2017).
 - [64] Y.-J. Lin, K. Jiménez-García, and I. B. Spielman, *Nature* **471**, 83 (2011).

Supplemental Material

In-situ tunneling control in photonic potentials by Rashba-Dresselhaus spin-orbit coupling

Rafał Mirek,^{1,*} Pavel Kokhanchik,^{2,*} Dariusz Urbonas,¹ Ioannis Georgakilas,¹ Marcin Muszyński,³ Piotr Kapuściński,³ Przemysław Oliwa,³ Barbara Piętka,³ Jacek Szczytko,³ Michael Forster,⁴ Ullrich Scherf,⁴ Przemysław Morawiak,⁵ Wiktor Piecek,⁵ Przemysław Kula,⁶ Dmitry Solnyshkov,^{2,7} Guillaume Malpuech,² Rainer F. Mahrt,¹ and Thilo Stöferle¹

¹IBM Research Europe - Zurich, Säumerstrasse 4, Rüschlikon, Switzerland[†]

²Université Clermont Auvergne, Clermont Auvergne INP, CNRS, Institut Pascal, F-63000 Clermont-Ferrand, France

³Institute of Experimental Physics, Faculty of Physics, University of Warsaw, Poland

⁴Macromolecular Chemistry Group and Wuppertal Center for Smart Materials & Systems (CM@S), Bergische Universität Wuppertal, Gauss Strasse 20, 42119 Wuppertal, Germany

⁵Institute of Applied Physics, Military University of Technology, Warsaw, Poland

⁶Institute of Chemistry, Military University of Technology, Warsaw, Poland

⁷Institut Universitaire de France (IUF), 75231 Paris, France

SAMPLE STRUCTURE

The sample consists of two dielectric mirrors formed by a distributed Bragg reflector (DBR) deposited on a 3 mm thick quartz substrate with a 30 nm thick ITO electrode. Each DBR is made of 7.5 Ta₂O₅/SiO₂ pairs using ion beam deposition. On one of the DBRs, we spin-coated a 40 nm layer of methyl-substituted ladder-type poly(p-phenylene) (MeLPPP) and covered it with 40 nm of Al₂O₃ and 50 nm of SiO₂ spacer. A polyimide layer (DL-3160 by Dalton) was spin-coated on top of the spacer, thermally cured, and then unidirectionally rubbed to serve as an orienting layer for the liquid crystal slab. The second DBR contains artificial Gaussian traps forming ST and DT structures. They were created on the glass substrate with an additional SiO₂ layer before the deposition of the mirror using focused ion beam milling [1]. The studied ST was 1.53 μm full width at half maximum (FWHM), and the DT potential consisted of two Gaussian traps having FWHM of 1.4 μm and 0.96 μm center-to-center distance. Both structures were etched to a depth of 40 nm. Finally, both cavity halves were merged and filled with high birefringence (Δ=0.43) liquid crystal 2091 (HBNLC). The spacing and sealing were performed

in the same way as in [2].

MEASUREMENT SETUP

The experimental setup is presented in Fig. S1. White light emitted from the halogen lamp and transmitted through the 10 μm diameter fiber (NA = 0.1) is focused on the sample using 50x microscope objective with numerical aperture (NA) = 0.75. The FWHM of the focused beam spot is of around 6 μm. The light transmitted through the sample is collected using 10x microscope objective (NA = 0.3) and directed on the imaging spectrograph. We use 0.5 m long monochromator with 300 lines/mm grating. The half-wave plate (λ/2), quarter-wave plate (λ/4) and linear polarizer (lin) are used for detecting light of different polarization. The lenses are used for imaging of real space (x) and momentum space (x and k).

TIGHT-BINDING MODEL

The 6x6 tight-binding Hamiltonian describing DT localized states written in the basis ($|H_s^e\rangle |H_s^o\rangle |V_s^e\rangle |V_s^o\rangle |H_p^e\rangle |V_p^e\rangle$)^T reads as:

$$H_{DT}^{(6)} = \begin{pmatrix} E_{H_s^e} & 0 & 0 & i\beta_{DT,1} & 0 & 0 \\ 0 & E_{H_s^o} & -i\beta_{DT,1} & 0 & 0 & -i\beta_{DT,2} \\ 0 & i\beta_{DT,1} & E_{V_s^e} + \delta & 0 & 0 & 0 \\ -i\beta_{DT,1} & 0 & 0 & E_{V_s^o} + \delta & -i\beta_{DT,3} & 0 \\ 0 & 0 & 0 & i\beta_{DT,3} & E_{H_p^e} & 0 \\ 0 & i\beta_{DT,2} & 0 & 0 & 0 & E_{V_p^e} + \delta \end{pmatrix}, \quad (S1)$$

with E_φ energy of the localized state $|\varphi\rangle$, δ linear po-

larization detuning, $\beta_{DT,1} = |\langle H_s^e | 2\alpha k_x | V_s^o \rangle|$, $\beta_{DT,2} =$

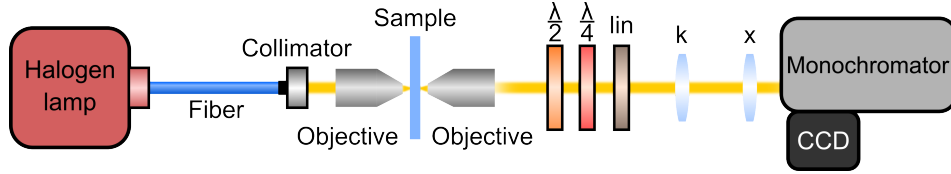


Figure S1. Experimental setup for polarisation-resolved white light transmission experiments.

$|\langle H_s^o | 2\alpha k_x | V_p^e \rangle|$ and $\beta_{DT,3} = |\langle V_s^o | 2\alpha k_x | H_p^e \rangle|$ RDSOC matrix elements. The tunneling coefficient between ST localized states $|H_s\rangle$ in the case of zero RDSOC is defined as $j_0 = (E_{H_s^o} - E_{H_s^e})/2$, while the degenerate eigenenergies of these states are $E_{H_s} = (E_{H_s^o} + E_{H_s^e})/2$.

After applying 2nd order perturbation theory in the limit $|\delta| \gg \max|\Delta E_{ij}|, \beta, |j_0|$, where ΔE_{ij} is the difference between i th and j th localized states, we reduce Hamiltonian (S1) to an effective 2x2 Hamiltonian including only $(|H_s^l\rangle |H_s^r\rangle)^T$ basis states (left and right wells in DT):

$$H_{DT} = \begin{pmatrix} E'_{H_s}(\delta) & -j(\delta) \\ -j(\delta) & E'_{H_s}(\delta) \end{pmatrix}, \quad (S2)$$

with $E'_{H_s}(\delta) = E_{H_s} - \beta_{DT,1}^2/(E_{V_s} - E_{H_s} + \delta) - \beta_{DT,2}^2/[2(E_{V_p^e} - E_{H_s} + \delta)]$ detuning-dependent modified energy of ST state $|H_s\rangle$, and $j(\delta) = j_0 - \beta_{DT,2}^2/[2(E_{V_p^e} - E_{H_s} + \delta)]$ detuning-dependent effective tunneling. Left-right site basis $(|H_s^l\rangle |H_s^r\rangle)^T$ is related to the even-odd DT state basis $(|H_s^e\rangle |H_s^o\rangle)^T$ through the 2x2 Hadamard matrix.

CALCULATION PARAMETERS

The potentials used for ST and DT simulations are, respectively:

$$U_{H,V}(x) = -A_{H,V} \exp\left[-\frac{x^2}{2\sigma^2}\right], \quad (S3)$$

$$U_{H,V}(x) = -A_{H,V} \times \left(\exp\left[-\frac{(x-d/2)^2}{2\sigma^2}\right] + \exp\left[-\frac{(x+d/2)^2}{2\sigma^2}\right] \right), \quad (S4)$$

with $A_{H,V}$ potential depth for H,V polarization, σ potential width, d intersite distance in DT. The parameters used in the simulation are the following:

Figs. 1-2. Numerical simulation: $\alpha = 2 \text{ meV}\cdot\mu\text{m}$, $m_H = 1.8 \cdot 10^{-5}m_e$, $m_V = 2.3 \cdot 10^{-5}m_e$, $\sigma = 0.54 \mu\text{m}$, $A_H = 36.64 \text{ meV}$, $A_V = 9.41 \text{ meV}$. Tight-binding: $E_{H_s} = -25.8 \text{ meV}$, $E_{H_p} = -9.5 \text{ meV}$, $E_{V_s} = -5.2 \text{ meV}$, $E_{V_p} = 1.5 \text{ meV}$, $\beta_{ST,1} = 7 \text{ meV}$, $\beta_{ST,2} = 5 \text{ meV}$.

Fig. 3. Numerical simulation: $\alpha = 2.4 \text{ meV}\cdot\mu\text{m}$, $m_H = 1.8 \cdot 10^{-5}m_e$, $m_V = 2.3 \cdot 10^{-5}m_e$, $\sigma = 0.45 \mu\text{m}$, $A_H = 32.50 \text{ meV}$, $A_V = 17.73 \text{ meV}$, $d = 1.17$

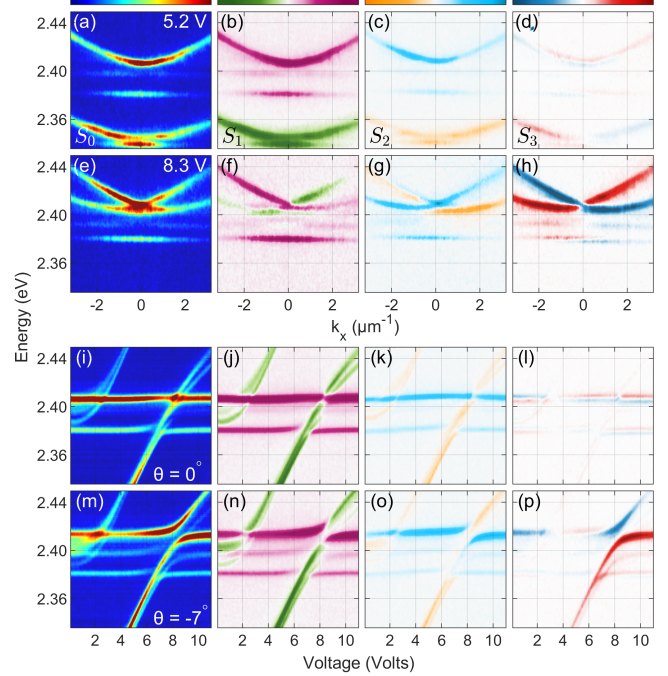


Figure S2. **Stokes parameters of ST.** Columns (from left to right): Intensity S_0 and Stokes parameters S_{1-3} ; Rows (from top to bottom): (a-d) dispersion for 5.2 V (big linear detuning δ), (e-h) dispersion for 8.3 V (small linear detuning δ), (i-l) energy-voltage diagram for detection angle $\theta = 0^\circ$, (m-p) energy-voltage diagram for detection angle $\theta = -7^\circ$.

μm . Tight-binding: $j_0 = 4.28 \text{ meV}$, $\beta_{DT,2} = 6.86 \text{ meV}$, $E_{V_p^e} - E_{H_s} = 7.54 \text{ meV}$.

Fig. 4. $\delta = 20 \text{ meV}$, $m_H = 1.8 \cdot 10^{-5}m_e$, $m_V = 2.3 \cdot 10^{-5}m_e$, $\sigma = 0.38 \mu\text{m}$, $A_H = 32.50 \text{ meV}$, $A_V = 17.73 \text{ meV}$, $d = 1.30 \mu\text{m}$.

* These authors contributed equally to this letter.

† rafal.mirek@ibm.com

- [1] L. Mai, F. Ding, T. Stöferle, A. Knoll, B. J. Offrein, and R. F. Mahrt, Applied Physics Letters **103** (2013).
- [2] K. Rechcińska, M. Król, R. Mazur, P. Morawiak, R. Mirek, K. Łempicka, W. Bardyszewski, M. Matuszewski, P. Kula, W. Piecek, *et al.*, Science **366**, 727 (2019).

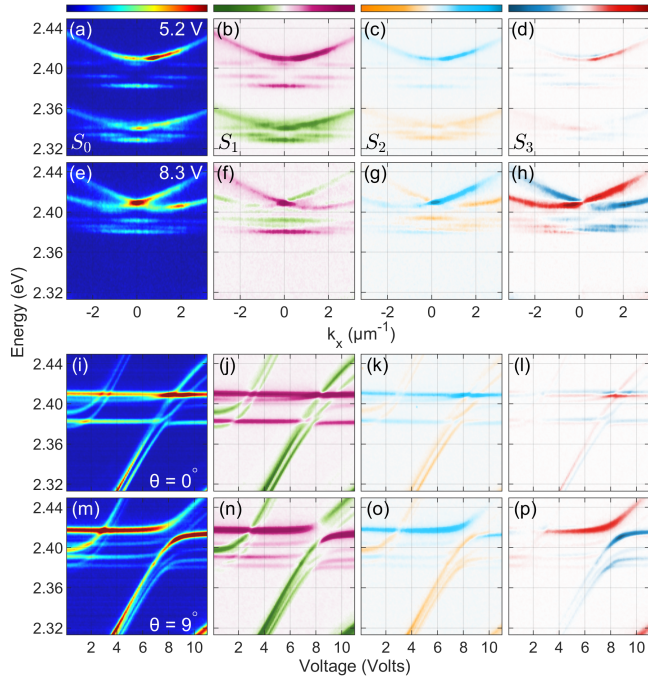


Figure S3. **Stokes parameters of DT.** Columns (from left to right): Intensity S_0 and Stokes parameters S_{1-3} ; Rows (from top to bottom): (a-d) dispersion for 5.2 V (big linear detuning δ), (e-h) dispersion for 8.3 V (small linear detuning δ), (i-l) energy-voltage diagram for detection angle $\theta = 0^\circ$, (m-p) energy-voltage diagram for detection angle $\theta = 9^\circ$.